

# MECHANICAL PROPERTIES OF LOW-CARBON ENGINEERED CEMENTITIOUS COMPOSITES WITH LIMESTONE AND CALCINED CLAY UNDER UNIAXIAL CYCLIC COMPRESSION

WANG KAICHUANG<sup>\*</sup>, ZHOU JIAJIA<sup>†</sup>, AND ZHAO JUN<sup>‡</sup>

<sup>\*</sup> Zhengzhou University, School of Mechanics and Safety Engineering  
Zhengzhou, China

e-mail: 981517326@qq.com, www.zzu.edu.cn

<sup>†</sup> Zhengzhou University, School of Mechanics and Safety Engineering  
Zhengzhou, China

e-mail: zhouaf@zzu.edu.cn, www.zzu.edu.cn

<sup>‡</sup> Zhengzhou University, School of Civil Engineering  
Zhengzhou, China

e-mail: zhaoj@zzu.edu.cn, www.zzu.edu.cn

**Key words:** LCC-ECC, Uniaxial cyclic compression, Stress-strain curve, Stiffness degradation, Damage constitutive model

**Abstract:** It is crucial to investigate the cyclic compression performance of low-carbon engineered cementitious composites (ECC) with limestone and calcined clay (LCC) during earthquakes. In this paper, the effects of water-binder ratios and replacement rates of LCC were investigated on the mechanical properties of LCC-ECC under uniaxial cyclic compression. The failure mode was observed, and the law of the stress-strain curves was summarized. The influences of the water-binder ratio and LCC substitution rate on the stress degradation, stiffness degradation, and hysteretic energy dissipation were analyzed for specimens subjected to uniaxial cyclic compressive loading. The results showed that reducing water-binder ratio can effectively decrease the stiffness degradation and hysteretic energy dissipation, but had little effect on the stress degradation. The replacement rate of LCC significantly affected the stress degradation, stiffness degradation, and hysteretic energy dissipation of the specimens. In particular, the ductility and energy dissipation of the specimens were notably improved at a 50% substitution rate. Finally, a damage constitutive model for LCC-ECC under uniaxial cyclic compression is proposed. The model accurately predicted the unloading path, reloading path, residual strain development, and damage evolution of LCC-ECC.

## 1 INTRODUCTION

Due to the brittle nature, low tensile strength and poor toughness of concrete, it is prone to mechanical performance degradation in harsh environments, which seriously affects the durability and safety of concrete structures and shortens the service life of engineering

structures. To address these issues, Li et al. [1-3] developed a novel fiber-reinforced engineered cementitious composite (ECC) based on micromechanics and fracture mechanics principles. When the fiber volume content is only 2%, ECC material exhibits multi-crack and strain hardening behavior

under tensile load., with crack widths typically less than 100  $\mu\text{m}$  [4] and its ultimate tensile strain can reach 8%, which is hundreds of times that of ordinary concrete [5-6]. Compared to traditional concrete, ECC not only exhibits extraordinary deformability but also superior durability, making it more suitable for infrastructure construction in harsh environments. However, due to the absence of coarse aggregate in ECC, cement is essential as a raw material during its preparation. It is well known that the production of cement releases a significant amount of carbon dioxide, accounting for 6-7% of global greenhouse gas emissions [7], which has a considerable negative impact on the environment. Therefore, reducing the use of cement and exploring alternative materials has become crucial strategies for decreasing carbon footprint and addressing climate change.

Researchers have tried to use industrial waste, such as ground granulated blast furnace slag (GGBS) [8], fly ash [9], geopolymers [10] and recycled glass powder (RGP) [11], to replace part of cement in the preparation of green cementitious materials, making significant progress. In this context, Scrivener [12] proposed that metakaolin and limestone (LCC) are also alternative materials for green cement. During the production of raw materials, LCC consumes less energy and emits less carbon dioxide than traditional cement [13]. During the concrete forming process, the alumina and silica in metakaolin react with calcium hydroxide from cement hydration products to form new hydration products C-A-S-H [14], and limestone reacts with calcium hydroxide to promote the formation of more C-S-H gel, thereby optimizing the cement hydration process and improving the microstructure of concrete.

Given the feasibility of using limestone calcined clay (LCC) as a cement substitute, studies have begun to explore its application in engineered cementitious composites (ECC) to develop green ECC materials. Zhang et al. [15] and Zhu et al. [16] conducted the first research on LCC-ECC. By optimizing the mix design of LCC-ECC, it was found that LCC-based ECC exhibits fine cracks, excellent self-

healing ability and higher tensile strain capacity under tensile load. Moreover, the addition of LCC reduces the energy consumption and carbon emissions of ECC, contributing to its environmental benefits. Additionally, LCC exhibits unique thixotropy, high yield stress and high plastic viscosity, enhancing its suitability for 3D printing construction [17] and sprayable repair engineering [18].

Due to the high ductility and low carbon characteristics of LCC-ECC, it has broad application prospects in low-carbon engineering structures under severe conditions. Structures that incorporate LCC-ECC are susceptible to cyclic loading, such as that induced by seismic events. Thus, precise constitutive models are required to predict their mechanical behavior under seismic loading, which is essential for designing relevant structural components. However, existing studies have primarily focused on the experimental investigation of the fundamental mechanical properties of LCC-ECC materials, with little research on predicting their mechanical behavior. Currently, only Huang et al. [19] established a bilinear constitutive model of LCC-ECC material under static compression load. Therefore, this study investigates the effects of different water-binder ratios and LCC contents on material stress degradation, stiffness degradation and hysteretic energy dissipation through uniaxial compression cyclic tests. A damage evolution-based constitutive model is proposed to predict the mechanical behavior of LCC-ECC structural components under cyclic and seismic loads. To mitigate the environmental impact of silica sand extraction and transportation, this study uses manufactured sand as the fine aggregate.

## 2 EXPERIMENTAL DESIGN

### 2.1 Mix proportions

The basic materials used in the experiment for LCC-ECC include 52.5 Ordinary Portland Cement, silica fume, metakaolin, and limestone, and their particle size distribution

was shown in figure 1. The length of PE fiber is 12 mm, the diameter is 24  $\mu\text{m}$ , the tensile strength is 3000 MPa, the density is 0.97g/cm<sup>3</sup>, and the volume fraction of PE fiber is 2%. The objective of this study is to investigate the effects of LCC content and water-to-binder ratio on the cyclic compressive performance of LCC-ECC. To achieve this, the experiments were designed with five different water-to-binder ratios (0.20, 0.28, 0.35, 0.45, 0.55) and four LCC contents (0, 0.3, 0.45, 0.6). The specific mix proportions are detailed in Table 1.

**Table 1:** Mixture proportions

Specimens	Cement and silica fume	Calcined clay and limestone	Water	PE fiber
W0.20-LCC0.45	0.55	0.45	0.2	2%
W0.28-LCC0.45	0.55	0.45	0.28	2%
W0.35-LCC0.45	0.55	0.45	0.35	2%
W0.45-LCC0.45	0.55	0.45	0.45	2%
W0.55-LCC0.45	0.55	0.45	0.55	2%
W0.28-LCC0	1	0	0.28	2%
W0.28-LCC0.30	0.70	0.30	0.28	2%
W0.28-LCC0.60	0.40	0.60	0.28	2%

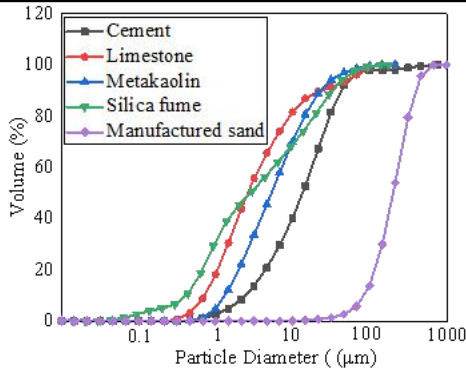


**Figure 1:** Particle size distribution of cementitious materials and manufactured sand

## 2.2 Test units and loading procedure

The loading device is composed of MTS actuator and load sensor, as shown in Figure 2. The loading system of LCC-ECC cyclic loading is shown in Figure 3. First, cyclic preloading was performed to load to 30 kN at a rate of 1kN/s, and then unloaded to 1kN at the same rate for three times to reduce the gap between the specimen and the machine and inside the specimen. The formal loading adopts graded cyclic loading. In the linear elastic stage, the displacement increases by 0.15 mm for one loading and unloading cycle. When the peak stress is reached, the

displacement increases by 0.4 mm for one loading and unloading cycle. Each stage of loading is carried out at a rate of 0.5mm/min, and the unloading rate is 5kN / s to 1kN. When the machine displacement reached 4.8 mm, the specimen was monotonically loaded at a rate of 0.3 mm / min until failure.



**Figure 2:** Loading device

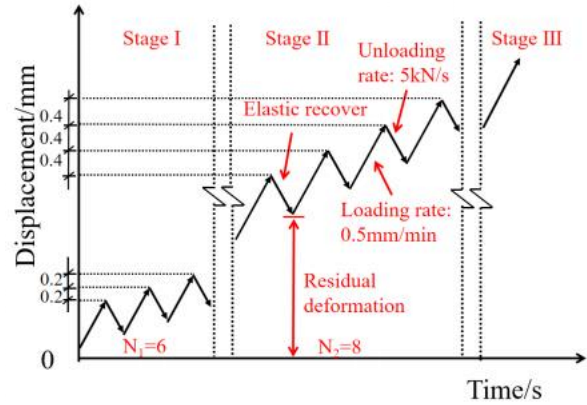


**Figure 3:** Uniaxial reciprocating compression loading system

## 3 RESULT AND DISCUSSION

### 3.1 Failure mode

Figure 4 shows the failure mode of LCC-ECC specimens under reciprocating compression load. It is shown in the figure that the failure modes of LCC-ECC specimens with different ratios are similar, showing the characteristics of shear failure. The main crack has a dip angle of 30°-45° with the normal direction of the loading plane., accompanied by the formation of a large number of fine cracks. The main crack is caused by the local shear stress concentration caused by reciprocating compression and extends along the direction of maximum shear stress. The high density distribution of fine cracks benefits

from the bridging effect of the internal fibers of LCC-ECC, which effectively controls the propagation of cracks. Due to the bridging effect of fibers, the overall morphology of LCC-ECC remains intact when the specimen is destroyed, and no outward spalling occurs, which belongs to ductile failure.



Figure 4: Failure modes of LCC-ECC specimens

### 3.2 Stress-strain curve

The stress-strain curve of LCC-ECC under cyclic loading is shown in Figure 4. From the diagram, it can be seen that the cyclic compression curve of LCC-ECC shows similar characteristics to that of ordinary concrete. The stress-strain curve consists of three parts : loading stage, unloading stage and reloading stage. The reloading stage consists of multiple feature points. These feature points include : the unloading point  $(\varepsilon_{ui}, \sigma_{ui})$  to reach the specified displacement, the residual point (corresponding to the residual strain) when the unloading stress is zero  $(\varepsilon_{pi}, \sigma_{pi})$ , the intersection point of the unloading curve and the reloading curve  $(\varepsilon_{ci}, \sigma_{ci})$ , and the end point  $(\varepsilon_{ri}, \sigma_{ri})$  from the residual point to the tangent and coincidence of the envelope.

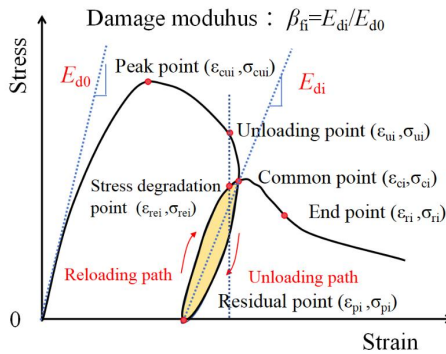


Figure 4: Feature points on unloading and reloading

paths

It can be seen from Figure 5 that the stress-strain curve shows that at the initial stage of loading, the reloading section and the unloading section are almost straight and coincide. During the loading and unloading process before the peak load, the LCC-ECC specimen shows obvious elastic characteristics. The unloading curve is highly coincident with the reloading curve. The elastic modulus of the reloading stage does not change significantly, and the residual strain is basically 0. However, after reaching the peak load, with the increase of the number of cycles, the slope of the reloading curve and the unloading curve gradually decreases, and the unloading curve shows an outward convex shape, showing significant nonlinear characteristics.

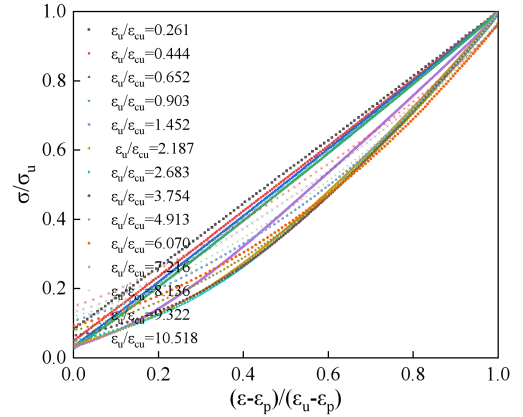
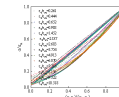


Figure 5: The stress-strain curve of LCC-ECC under cyclic loading.

Figure 6 shows the relationship between the unloading point and the stress degradation point. The stress degradation rate is defined as the ratio of the stress at the point with the same strain on the reloading curve to the stress at the unloading point during each loading and unloading process. The stress degradation degree of unloading and reloading paths can be characterized by the stress degradation rate, which is defined as :



$$(1)$$

In the formula,  $\varphi$  is the  $i$ th stress degradation rate,  $\sigma_{rei}$  is the stress on the reloading path corresponding to the unloading strain in the first  $i$ th loading and unloading, and  $\sigma_{ui}$  is the corresponding unloading stress.

It can be seen from the figure that the stress degradation process of LCC-ECC specimens with different proportions can be divided into two stages: rapid decline and stability. During the loading and unloading process before the peak stress, the specimen remains elastic, the stress degradation rate is close to 1.0, and the stress degradation phenomenon is not obvious. In the first loading and unloading cycle after the peak load, the curve shows a sharp drop, indicating that the stress degradation occurs at this time. In the subsequent loading and unloading cycles, the fluctuation of stress degradation rate is small and remains relatively stable. For example, with the increase of water-binder ratio, the minimum values of stress degradation rate are 80.2 %, 83.4%, 78.4%, 80.3% and 83.5%, respectively. With the increase of LCC content, the minimum stress degradation rates are 79.4%, 79.6%, 83.4% and 80.9%, respectively

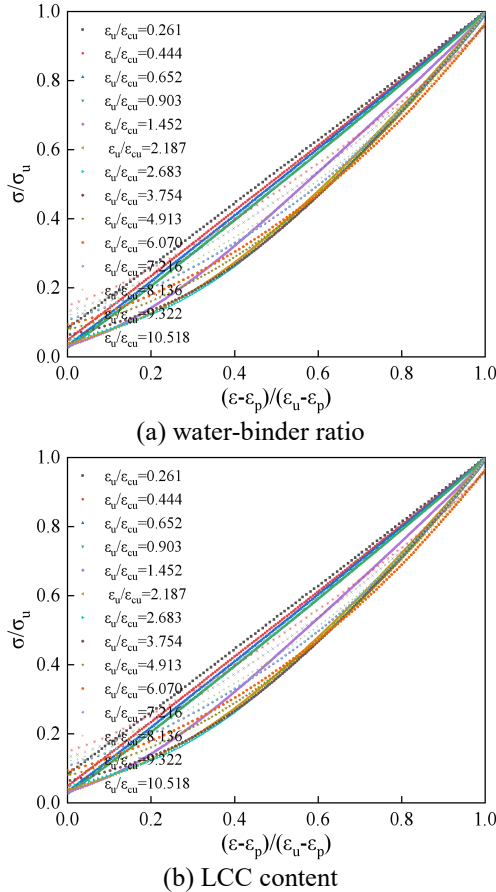
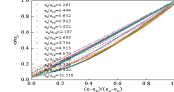


Figure 6: Stress degradation of LCC-ECC under different parameters

### 3.3 Unloading stiffness

In this paper, the elastic stiffness ratio

$(E_u/E_0)$  is used to quantify the stiffness degradation process of the LCC-ECC specimen, where  $E_0$  is the initial stiffness of the LCC-ECC specimen, that is, the maximum unloading stiffness during the loading and unloading process before the peak stress. The unloading stiffness  $E_u$  is the slope of the straight line between the unloading point and the residual strain point in each cycle, which is calculated by formula (2).



(2)

In the formula,  $\sigma_{pi}$  is the residual stress,  $\epsilon_{pi}$  is the residual strain,  $\sigma_{ui}$  is the unloading point stress, and  $\epsilon_{ui}$  is the unloading point strain.

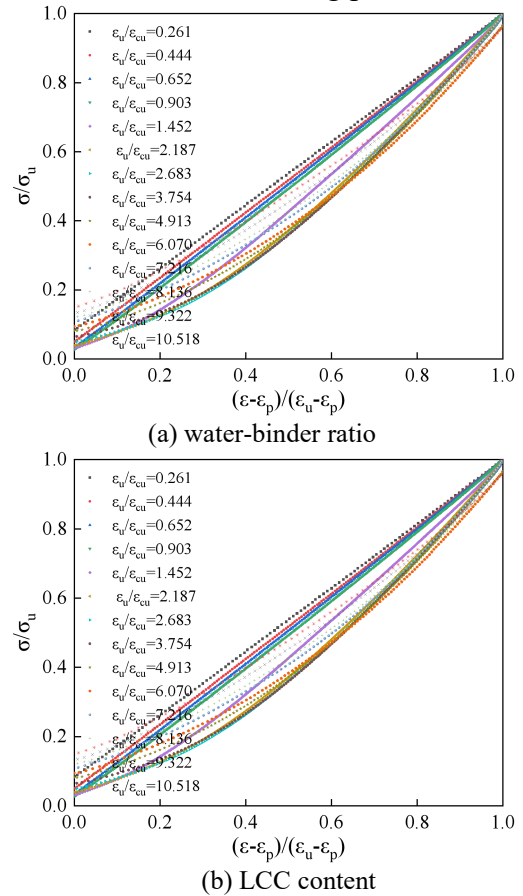


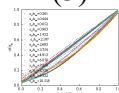
Figure 7: The stiffness degradation of LCC-ECC under different parameters

It can be seen from the Figure 7 that as the number of loading and unloading cycles increases, the unloading stiffness of the specimen gradually decreases, indicating that the elastic recovery ability of the material under repeated loading gradually decreases. The water-binder ratio has a significant effect on the stiffness degradation, and the greater

the water-binder ratio, the faster the stiffness degradation of the specimen. When the LCC-ECC specimen is loaded to failure, the stiffness degradation rate is 63.35%, 62.11%, 62.01%, 58.57% and 58.95% respectively with the increase of water-binder ratio. This is because when the water-binder ratio is large, there are many initial defects inside LCC-ECC, and the initial elastic modulus is small. With the increase of the number of reciprocating loadings, the microcracks continue to expand and penetrate each other, and the plastic deformation continues to accumulate, resulting in the gradual accumulation of internal damage and the increase of irreversible deformation. As a result, the unloading stiffness is continuously reduced, and the unloading stiffness degradation is more serious. Compared with the specimens without LCC, the addition of LCC can reduce the stiffness degradation rate of the specimens, but the content of different LCC has little effect on the unloading stiffness. This is because the particle size of calcined clay and limestone without secondary hydration is small, which can fill the voids in the cement matrix and optimize its microstructure. To a certain extent, it can reduce the generation of internal micro-defects. Therefore, it can effectively slow down the accumulation of damage and reduce the degradation of stiffness under reciprocating compression.

### 3.2 Hysteresis strain energy

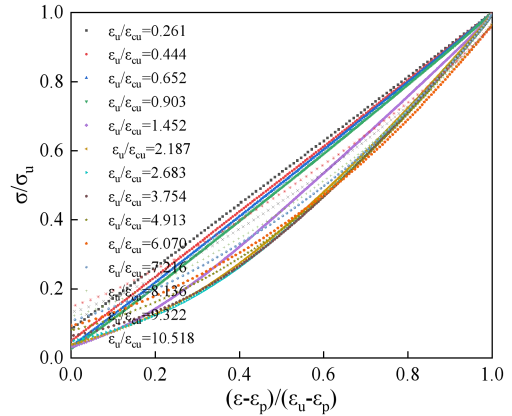
The area enclosed by the unloading and reloading stages of the two paths (the yellow area in figure 4) represents the hysteretic energy consumed during the unloading and reloading cycles. In this section, the relative energy dissipation ( $W_{ri}$ ) is used to evaluate the energy dissipation under cyclic compression, that is, the ratio of the hysteretic energy dissipation ( $W_i$ ) in each loading and unloading cycle to the maximum stress ( $\sigma_{ui}$ ) in the cycle, expressed in formula (3).



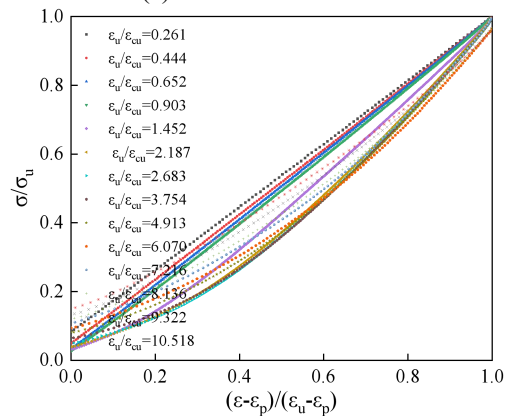
$$(3)$$

Figure 8 shows the variation curve of relative hysteretic energy consumption with

the number of cycles during each unloading and reloading process under different water-binder ratio and LCC content. It can be seen that the curve consists of ascending and descending segments. In the rising section, the relative hysteretic energy consumption increases rapidly with the increase of the number of cycles, and the curve of the rising section under different water-binder ratio and LCC content is small. In the falling period, the relative energy consumption decreases slowly with the increase of the number of cycles. With the increase of water-binder ratio, the hysteretic energy consumption per unit strength decreases gradually, and the maximum values are 0.477, 0.438, 0.344, 0.339 and 0.318 respectively. Compared with the specimens without LCC, the specimens with LCC have higher relative hysteretic energy consumption, but with the increase of LCC content, the influence on the relative energy consumption is not significant, and the maximum values are 0.457, 0.459 and 0.450, respectively.



(a) water-binder ratio



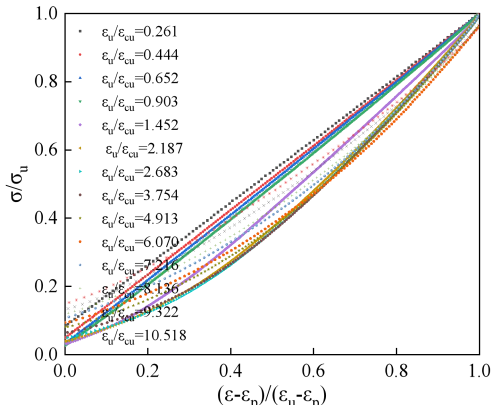
(b) LCC content

**Figure 8:** The relative energy dissipation of LCC-ECC under different parameters

## 4 DAMAGE MODEL

### 4.1 Relationship between residual and unloaded strains

Under cyclic loading, the LCC-ECC specimen undergoes a transition process from elastic deformation to plastic deformation. Xu et al. [20] used a power function to describe the relationship between the residual strain and the unloading point strain of steel-polypropylene hybrid fiber reinforced concrete (BFRC), and found that the model can better reflect the change process of the two. In this paper, it is found that the relationship between the residual strain and the unloading point strain of the LCC-ECC specimen can also be expressed in the form of a power function, as shown in formula (4).



$$\sigma/\sigma_u = \alpha \left( \frac{\epsilon - \epsilon_p}{\epsilon_u - \epsilon_p} \right)^\beta \quad (4)$$

In the formula,  $\epsilon_{ui}$  is the unloading point strain,  $\epsilon_{pi}$  is the residual strain,  $\epsilon_{cu}$  is the peak strain of the stress-strain curve of the specimen under cyclic loading,  $\alpha$  and  $\beta$  are the model parameters. The values of  $\alpha$  and  $\beta$  can be obtained by regression analysis of experimental data, as shown in table 2.

**Table 2:** Relationship between residual and unloaded strains.

Specimens	Peak stress ( $f_{cu}$ )	Model parameters		$R^2$
		$\alpha$	$\beta$	
W0.20-LCC0.45	75.1	0.677	1.157	0.995
W0.28-LCC0.45	56.9	0.588	1.193	0.996
W0.35-LCC0.45	53.6	0.59	1.22	0.995
W0.45-LCC0.45	47.1	0.587	1.284	0.998
W0.55-LCC0.45	30.6	0.537	1.346	0.993
W0.55-LCC0.45	61.6	0.537	1.229	0.996
W0.28-LCC0.30	61.3	0.551	1.219	0.997
W0.28-LCC0.60	56.1	0.55	1.22	0.997

Figure 9 shows the comparison between the experimental data and the theoretical results of each group of specimens. It can be seen from the figure that under the influence of water-binder ratio and LCC content, the relationship between residual strain and unloading strain shows nonlinear characteristics. From Figure 9 and Table 2, it can be seen that the model is in good agreement with the experimental results, and the correlation coefficient  $R^2$  of each

group of specimens is between 0.995 and 0.998.

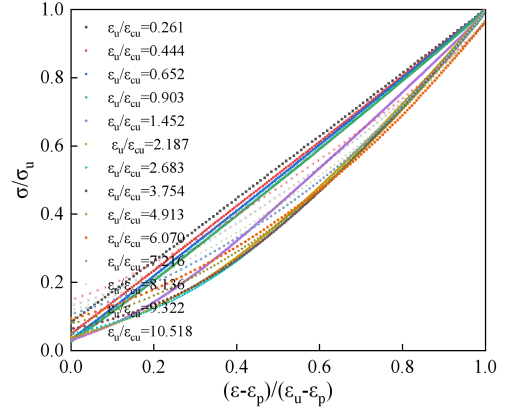
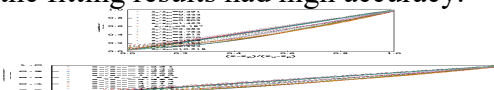


**Figure 9:** Relation between reloading strain and residual strain.

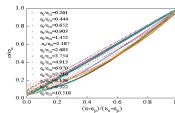
Since the effect of LCC content on residual strain is not significant, the effect of LCC content can be ignored when establishing the relationship between plastic strain and unloading point strain. Based on the experimental data of different water-binder ratios in Table 2, the relationship between peak load and residual strain is established, which is expressed by Equation (5) and (6). In the fitting results, the correlation coefficients  $R^2$  of the model parameters  $\alpha$  and  $\beta$  were 0.9614 and 0.9998, respectively, indicating that the fitting results had high accuracy.



$$\sigma/\sigma_u = \alpha \left( \frac{\epsilon - \epsilon_p}{\epsilon_u - \epsilon_p} \right)^\beta \quad (5)$$

### 4.2 Relationship between residual and reloaded strains

It can be seen from Fig.6 that the residual strain point ( $\epsilon_{pi}$ ,  $\sigma_{pi}$ ) is loaded again until it coincides with the envelope line, and the coordinates of the point are ( $\epsilon_{ri}$ ,  $\sigma_{ri}$ ). Figure 10 shows the relationship between residual strain and reloading strain of LCC-ECC specimens under different influencing factors. Based on these changes, a power function model in the same form as the unloading section is proposed, which is expressed by Equation (7). Through regression analysis of the test results, the model parameters  $\gamma$  and  $\theta$  of each group of specimens are shown in table 3.



$$\sigma/\sigma_u = \alpha \left( \frac{\epsilon - \epsilon_p}{\epsilon_u - \epsilon_p} \right)^\beta \quad (7)$$

Where  $\varepsilon_{cu}$  is the peak strain of the stress-strain curve of the specimen under cyclic loading.  $\gamma$  and  $\theta$  are model parameters.

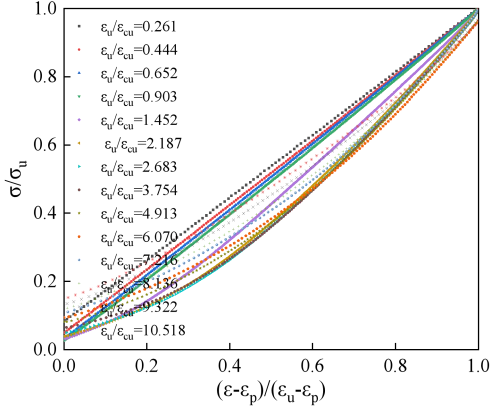


**Figure 10:** Relation between reloading strain and residual strain.

It can be seen from Figure 10 that the relationship between reloading strain and residual strain presents a nonlinear mode. The water-binder ratio significantly affects the relationship between reloading strain and residual strain, while the LCC content has no significant effect on the residual strain of LCC-ECC specimens, and the model parameters  $\gamma$  and  $\theta$  of the specimens change little. Therefore, the influence of LCC content can be ignored when establishing the relationship between reloading strain and residual strain. The model matched the experimental results well, with  $R^2$  values for each group ranging from 0.978 to 0.993.

**Table 3:** Relationship between reloaded and residual strains.

Specimens	Peak stress ( $f_{cu}$ )	Model parameters		$R^2$
		$\gamma$	$\theta$	
W0.20-LCC0.45	75.1	1.468	0.856	0.995
W0.28-LCC0.45	56.9	1.981	0.75	0.996
W0.35-LCC0.45	53.6	1.766	0.767	0.995
W0.45-LCC0.45	47.1	1.682	0.667	0.998
W0.55-LCC0.45	30.6	1.071	0.691	0.993
W0.55-LCC0.45	61.6	2.093	0.739	0.996
W0.28-LCC0.30	61.3	2.002	0.749	0.997
W0.28-LCC0.60	56.1	2.017	0.738	0.997

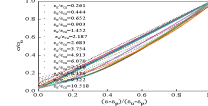
According to the test data of different water-binder ratios shown in Table 3, the relationship between peak load and residual strain was established. The model parameters  $\gamma$  and  $\theta$  of each group of LCC-ECC specimens were determined and expressed in formulas (8) and (9). The  $R^2$  of the fitting model parameters  $\gamma$  and  $\theta$  were 0.9693 and 0.9523, respectively, indicating that the fitting results were ideal.

$$(8)$$

$$(9)$$

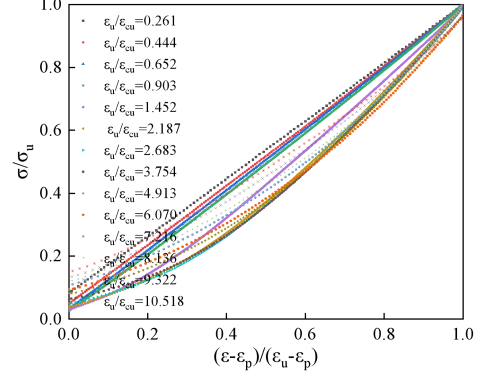
### 4.3 Unloading stress-strain equations

For LCC-ECC materials, the unloading stage can be fitted by power function. Since the influence of LCC content on the curve is not significant, the influence of LCC content is not considered when establishing the equations of unloading section and reloading section, and only the stress-strain relationship of LCC-ECC specimens under different water-binder ratios is studied. As shown in Figure 11, the shape of the unloading curve is represented by  $\varepsilon-\varepsilon_p/\varepsilon_u-\varepsilon_p$  as the horizontal axis and  $\sigma/\sigma_u$  as the vertical axis. The experimental curves and theoretical curves of the unloading stage under different ratios are shown in the figure. In this paper, the regression analysis is carried out by using the formula (10).

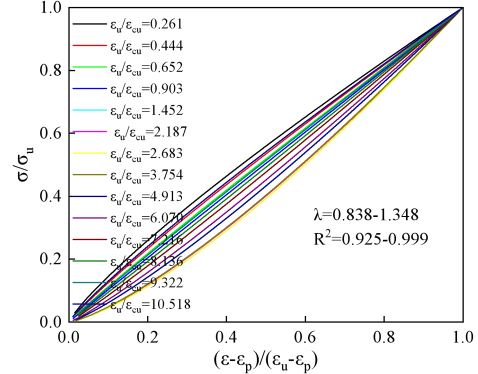


$$(10)$$

Where  $\sigma_{ui}$  is the stress at the  $i$ th unloading point.  $\lambda$  is the model parameter.



(a) Unloading experimental curves



(b) Unloading theoretical curves

**Figure 11:** Typical normalized unloading stress-strain curves.



It can be seen from Figure 15 that the stress of the specimen decreases rapidly at the initial stage of unloading. When the stress drops to 40%~60% of the unloading point stress ( $\sigma_u$ ), the rate of stress decline begins to slow down. By analyzing the value of the correlation coefficient  $R^2$ , it can be seen that the fitting function used by LCC-ECC specimens with different water-binder ratios in the unloading section has high fitting accuracy. The relationship between  $\lambda$  and  $\varepsilon_u/\varepsilon_{cu}$ , the fitting curve is shown in Figure 12, and the fitting function is formula (11).

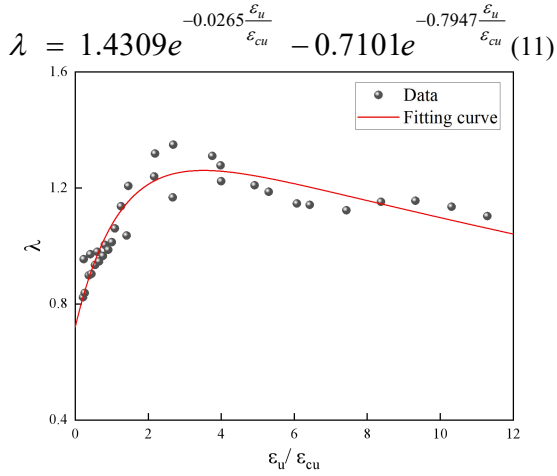


Figure 12: Relationship between  $\lambda$  and  $\varepsilon_u/\varepsilon_{cu}$

#### 4.4 Reloading stress-strain equations

Through the analysis of the curve shape of LCC-ECC in the reloading stage, it is found that the Fourier function fitting effect is better. Therefore, Formula (12) is used to predict the mechanical behavior of LCC-ECC specimens in the reloading stage. As shown in Figure 13, the shape of the reloading curve is represented by  $\varepsilon - \varepsilon_p/\varepsilon_r - \varepsilon_p$  as the horizontal axis and  $\sigma/\sigma_r$  as the vertical axis.

$$\frac{\sigma}{\sigma_r} = \mu + \eta \cdot \cos\left(\varphi \cdot \frac{\varepsilon - \varepsilon_{pi}}{\varepsilon_n - \varepsilon_{pi}}\right) + \kappa \cdot \sin\left(\varphi \cdot \frac{\varepsilon - \varepsilon_{pi}}{\varepsilon_n - \varepsilon_{pi}}\right) \quad (12)$$

It can be seen from Figure 13 that the stress of the specimen increases at the initial stage of reloading. When the stress reaches 80 % of the final loading point stress ( $\sigma_r$ ), the rate of stress increase begins to decrease. The values of these correlation coefficients  $R^2$  are greater than 0.95, indicating that the fitting function used in the reloading stage of LCC-ECC specimens with different water-binder ratios is

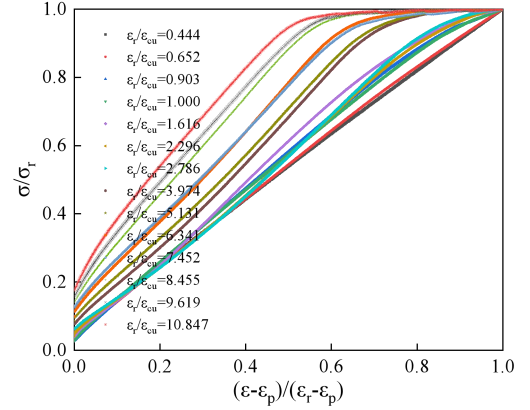
better. Figure 14 shows the relationship between the established model parameters  $\mu$ ,  $\eta$ ,  $\kappa$ ,  $\varphi$  and  $\varepsilon_r/\varepsilon_{cu}$ , and the fitting function is expressed by equations (13) to (16).

$$\mu = 0.7239e^{-0.0356\frac{\varepsilon_r}{\varepsilon_{cu}}} - 0.4039e^{-0.3984\frac{\varepsilon_r}{\varepsilon_{cu}}} \quad (13)$$

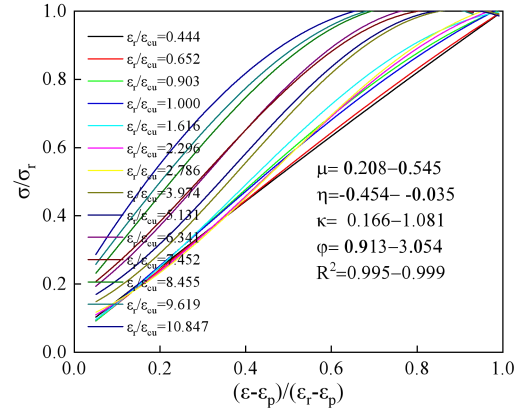
$$\eta = -0.4935e^{-0.0345\frac{\varepsilon_r}{\varepsilon_{cu}}} + 0.1965e^{-0.5776\frac{\varepsilon_r}{\varepsilon_{cu}}} \quad (14)$$

$$\kappa = 0.7953e^{-0.5782\frac{\varepsilon_r}{\varepsilon_{cu}}} + 0.0854e^{0.1427\frac{\varepsilon_r}{\varepsilon_{cu}}} \quad (15)$$

$$\varphi = 3.4318e^{-0.0317\frac{\varepsilon_r}{\varepsilon_{cu}}} - 2.8997e^{-0.6233\frac{\varepsilon_r}{\varepsilon_{cu}}} \quad (16)$$

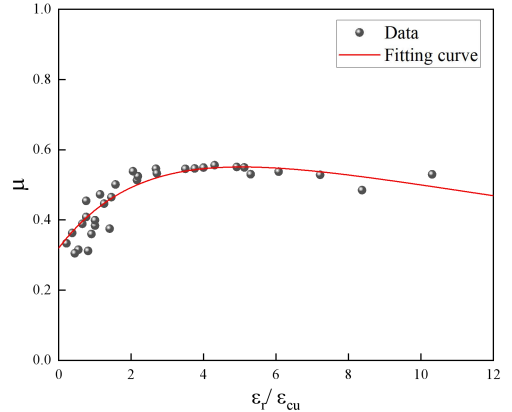


(a) Reloading experimental curves

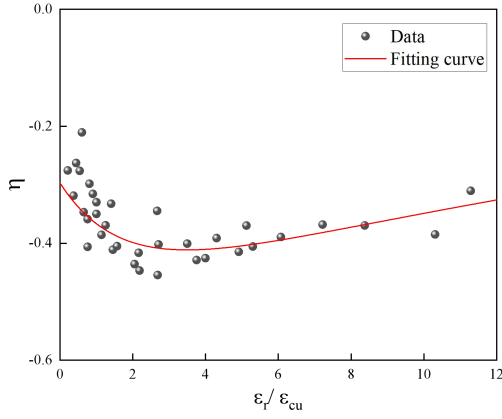
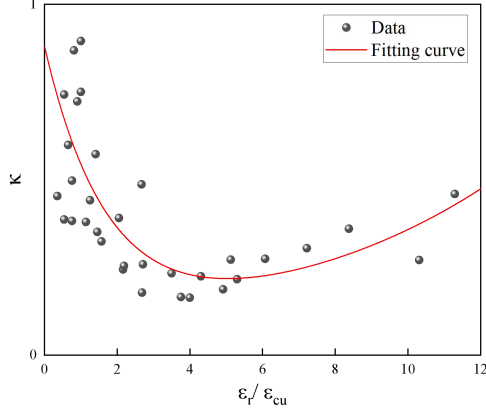
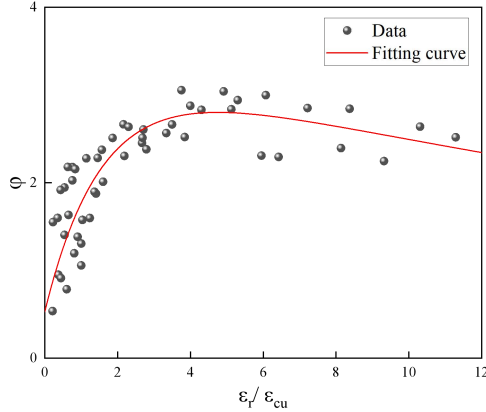


(b) Reloading theoretical curves

Figure 13: Typical normalized reloading stress-strain curves.



(a) Relationship between  $\mu$  and  $\varepsilon_r/\varepsilon_{cu}$


 (b) Relationship between  $\eta$  and  $\varepsilon_r/\varepsilon_{cu}$ 

 (c) Relationship between  $\kappa$  and  $\varepsilon_r/\varepsilon_{cu}$ 

 (d) Relationship between  $\varphi$  and  $\varepsilon_r/\varepsilon_{cu}$ 
**Figure 14:** The relationship between model parameters  $\mu$ ,  $\eta$ ,  $\kappa$ ,  $\varphi$  and  $\varepsilon_r/\varepsilon_{cu}$ .

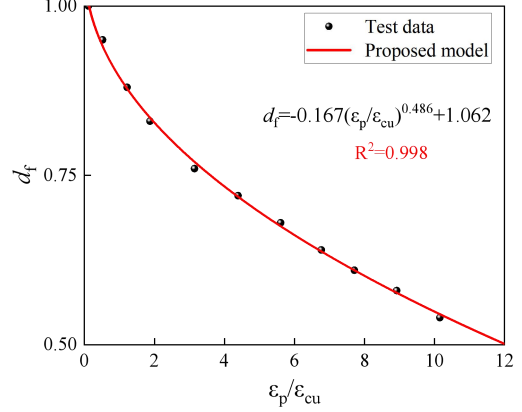
#### 4.4 Damage constitutive equation

During the loading process, cement-based materials usually show significant stiffness degradation, which is mainly caused by progressive damage accumulation. Therefore, the stiffness degradation process can be used as an effective means to characterize the damage evolution law. Based on the results of this experiment, combined with previous experimental data and models, the residual

strain was used as an independent variable to establish a damage modulus degradation factor model, as shown in Equation (17).

$$d_f = \chi \left( \frac{\varepsilon_{pi}}{\varepsilon_{cui}} \right)^\psi + \omega \quad (17)$$

In the formula,  $d_f$  is the degradation factor of damage modulus.  $\chi$ ,  $\psi$  and  $\omega$  are the model parameters of specimens, respectively.


**Figure 15:** Damage evolution models for LCC-ECC.

From Figure 15, it can be seen that the relationship function between residual strain and damage modulus is well fitted, and the correlation coefficient  $R^2$  is greater than 0.95, indicating that the model prediction value is highly consistent with the experimental results. In order to reflect the influence of water-binder ratio, the relationship between the model parameters and the peak load under different water-binder ratios is further established, as shown in formulas (18) to (20).

$$\chi = -0.0138f_{cu}^2 + 1.7995f_{cu} - 57.5807 \quad (18)$$

$$\psi = -20.1276f_{cu}^2 + 18.1505f_{cu} - 4.1582 \quad (19)$$

$$\omega = 0.0132f_{cu}^2 - 1.7241f_{cu} + 56.0804 \quad (20)$$

Figure 16 shows the stress-strain curve of the LCC-ECC specimen using the damage model proposed in this paper, and compares it with the existing model. It can be seen that in the unloading and reloading stages, due to the influence of complex factors such as test methods, equipment, crack propagation paths, and interface characteristics of the transition zone, the fitting results have certain errors. However, on the whole, the damage model proposed in this paper has a good fitting effect with the experimental data in the unloading and reloading stages. Compared with the damage model proposed by Chi et al. [21], the

damage model proposed in this paper shows higher accuracy in describing the curves of unloading and reloading stages under cyclic loading.

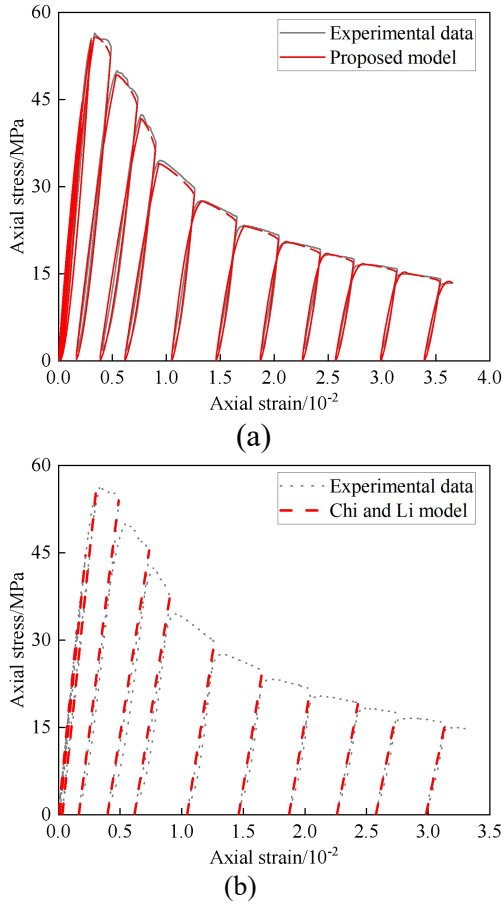


**Figure 16:** Comparison of the proposed model for stress-strain curves of unloading and reloading paths for LCC-ECC

## 5 CONCLUSIONS

The cyclic behavior of LCC-ECC was investigated in the present paper. The main findings are as follow:

(1) The failure modes of LCC-ECC specimens with different mix proportions are similar, characterized by shear failure. Fiber bridging ensures overall integrity during failure, exhibiting a ductile failure mode without spalling or outward fracturing.

(2) The stress degradation of LCC-ECC specimens has two stages. Before peak stress, the specimens remain elastic with minimal degradation. After peak load, a sudden sharp drop occurs, followed by stable stress degradation in subsequent cycles.

(3) Higher water-binder ratios significantly

accelerate stiffness degradation. Compared to specimens without LCC, adding LCC reduces the stiffness degradation rate, though different LCC contents have minimal impact on unloading stiffness.

(4) The relative hysteretic energy consumption curve consists of an ascending and a descending phase. In the ascending phase, relative energy consumption increases rapidly with the number of cycles, showing minimal variation across different water-binder ratios and LCC contents. Higher water-binder ratios lead to lower relative energy consumption. Specimens with LCC exhibit higher relative energy consumption than those without, but increasing LCC content has little impact on this trend.

(5) A new damage evolution model based on residual strain is proposed, considering the peak load. Additionally, a stress-strain constitutive model incorporating damage for LCC-ECC is developed. The model accurately predicts the unloading and reloading paths, residual strain progression, and damage evolution of the composite.

## REFERENCES

- [1] Li V C, Leung C K. Steady-state and multiple cracking of short random fiber composites[J]. *Journal of engineering mechanics*, 1992,118(11): 2246-2264.
- [2] Li V C, Stang H, Krenchel H. Micromechanics of crack bridging in fibre-reinforced concrete[J]. *Materials and structures*, 1993,26: 486-494.
- [3] Li V C. From micromechanics to structural engineering the design of cementitious composites for civil engineering applications[J]. *Doboku Gakkai Ronbunshu*, 1993, 1993(471): 1-12.
- [4] Yu J, Lu C, Chen Y, et al. Experimental determination of crack-bridging constitutive relations of hybrid-fiber Strain-Hardening Cementitious Composites using digital image processing[J]. *Construction and Building Materials*, 2018, 173: 359-367.
- [5] Chen Y, Yu J, Leung C K Y. Use of high

- strength strain-hardening cementitious composites for flexural repair of concrete structures with significant steel corrosion[J]. *Construction and Building Materials*, 2018, 167: 325-337.
- [6] He S, Qiu J, Li J, et al. Strain hardening ultra-high performance concrete (SHUHPC) incorporating CNF-coated polyethylene fibers[J]. *Cement and Concrete Research*, 2017, 98: 50-60.
- [7] Yu J. Multi-scale study on strain-hardening cementitious composites with hybrid fibers[M]. *Hong Kong University of Science and Technology*, 2021.
- [8] Kan L, Shi R, Zhu J. Effect of fineness and calcium content of fly ash on the mechanical properties of Engineered Cementitious Composites (ECC). *Construction and Building Materials*, 2019, 209: 476-484.
- [9] Özbay E, Karahan O, Lachemi M, et al. Dual effectiveness of freezing–thawing and sulfate attack on high-volume slag-incorporated ECC. *Composites Part B: Engineering*, 2013, 45(1): 1384-1390.
- [10] Shehab H K, Eisa A S, Wahba A M. Mechanical properties of fly ash based geopolymer concrete with full and partial cement replacement[J]. *Construction and building materials*, 2016, 126: 560-565.
- [11] Hisseine O A, Tagnit-Hamou A. Nanocellulose for ecological nanoengineered strain-hardening cementitious composites incorporating high-volume ground-glass pozzolans. *Cement and Concrete Composites*, 2020, 112: 103662.
- [12] Scrivener K, Martirena F, Bishnoi S, et al. Calcined clay limestone cements (LC3)[J]. *Cement and concrete research*, 2018, 114: 49-56.
- [13] Díaz Y C, Berriel S S, Heierli U, et al. Limestone calcined clay cement as a low-carbon solution to meet expanding cement demand in emerging economies[J]. *Development Engineering*, 2017, 2: 82-91.
- [14] Fernandez R, Martirena F, Scrivener K L. The origin of the pozzolanic activity of calcined clay minerals: A comparison between kaolinite, illite and montmorillonite[J]. *Cement and concrete research*, 2011, 41(1): 113-122.
- [15] Zhang D, Jaworska B, Zhu H, et al. Engineered Cementitious Composites (ECC) with limestone calcined clay cement (LC3)[J]. *Cement and Concrete Composites*, 2020, 114: 103766.
- [16] Zhu H, Zhang D, Wang T, et al. Mechanical and self-healing behavior of low carbon engineered cementitious composites reinforced with PP-fibers[J]. *Construction and Building Materials*, 2020, 259: 119805.
- [17] Zhou W, Zhu H, Hu W H, et al. Low-carbon, expansive engineered cementitious composites (ECC) in the context of 3D printing[J]. *Cement and Concrete Composites*, 2024, 148: 105473.
- [18] Zhu H, Yu K, Li V C. Sprayable engineered cementitious composites (ECC) using calcined clay limestone cement (LC3) and PP fiber[J]. *Cement and Concrete Composites*, 2021, 115: 103868.
- [19] Liang T, Chen L, Huang Z, et al. Ultra-lightweight low-carbon LC3 cement composites: Uniaxial mechanical behaviour and constitutive models[J]. *Construction and Building Materials*, 2023, 404: 133173.
- [20] L. Xu, B. Li, Y. Chi, C. Li, B. Huang, Y. Shi, Stress - Strain Relation of Steel - Polypropylene - Blended Fiber - Reinforced Concrete under Uniaxial Cyclic Compression[J]. *Advances in Materials Science and Engineering*, 2018, 2018(1): 9174943.
- [21] Li B, Xu L, Chi Y, et al. Experimental investigation on the stress-strain behavior of steel fiber reinforced concrete subjected to uniaxial cyclic compression[J]. *Construction and Building Materials*, 2017, 140: 109-118.